WILEY | Hindawi

Research Article

A Half-Cycle Negative-Stiffness Damping Model and Device Development

Tianwei Sun [ID],[1,2] Lingyun Peng [ID],[2] Xiaodong Ji,[1] and Xiaojun Li [ID][2]

[1]*Department of Civil Engineering, Tsinghua University, Beijing 100084, China*
[2]*Beijing Key Lab of Earthquake Engineering and Structural Retrofit, Beijing University of Technology, Beijing 100124, China*

Correspondence should be addressed to Lingyun Peng; ply@bjut.edu.cn

This paper proposes a novel damping model with negative stiffness known as the half-cycle negative-stiffness damping model. Analysis of a single degree of freedom (SDOF) system demonstrated that the half-cycle negative-stiffness damping model has negative stiffness and energy dissipation. The equivalent negative stiffness of the model was derived from the frequency response analysis of the system. An alternating transmission system and a one-way friction system were developed to assemble a half-cycle negative-stiffness damping device (HCNSDD), which can generate a half-cycle negative-stiffness damping model. A mechanical model was developed to represent the force-displacement relationship of the proposed HCNSDD. A HCNSDD specimen was manufactured and examined using experimental tests. The HCNSDD exhibits half-cycle negative-stiffness damping and stable mechanical properties, demonstrating the feasibility and effectiveness of the proposed HCNSDD. Finally, a finite element simulation approach for HCNSDD was presented, and the performance of seismic vibration control of HCNSDD was evaluated using a multidegree-of-freedom system.

1. Introduction

The objective of seismic protection is to reduce the force demand and control the lateral deformation of a structure subjected to strong ground motions. Extensive achievements have been made in this field, such as base isolation and energy dissipation technologies [1–8]. Due to their capacity to significantly reduce acceleration response, negative-stiffness vibration control techniques have been employed in civil engineering. Based on the mechanisms of negative stiffness, existing negative-stiffness technologies have primarily been categorized into the following: precompression springs [9, 10], negative-stiffness metamaterials [11], buckled beams [12], magnets [13], and magnetorheological technology [14]. In addition, the frequency-dependent negative-stiffness known as inerter [15] has gained notable attention. Smith [16, 17] introduced the concept of the ideal inerter and realized it by taking a plunger to drive a flywheel through a rack, pinion and gears. Garrido et al. [18] presented the concept of resettable-inertance inerter, which can show practical advantages such as higher energy

density and greater adaptability to energy harvesting applications.

Thus far, negative-stiffness technology has been extensively developed in mechanical engineering [19–21] and materials science fields [22–24]. Robertson et al. [25] used the arrangement of magnets to produce a negative-stiffness element to reduce the natural frequency of the system. Mehreganian et al. [26] investigated the negative-stiffness honeycomb metamaterials made of double curved beams. A negative-stiffness oscillator [27] was tested by Anastasio et al. This oscillator exhibits strong nonlinear behavior due to its polynomial elastic restoring force. Balasubramanian et al. [28–31] conducted experimental tests on plates and shells, which showed that the damping exhibits a major nonlinear nature related to vibration amplitude. They further confirmed the experimental observations of damping nonlinearity through discussions on the identified dissipation by different models. In addition, Amabili et al. [32–34] derived nonlinear damping for a continuous system and presented a procedure to identify the damping and stiffness coefficients of a nonlinear single-degree-of-freedom model.

Research in the field of civil engineering has shown that the use of negative-stiffness damping devices, which are developed based on the principles of friction and pre-compression springs, has a significant impact in reducing the vibrations of structures. In addition, the inerter-related damping devices that are characterized with frequency-dependent negative-stiffness feature have also gained notable attention. These devices can effectively control seismic vibrations in cables [35–38], bridges [39–41], isolation systems [42], outrigger tall buildings [43–46], and seismic protection of structures [47, 48].

Numerous studies have been conducted on negative-stiffness damping devices and associated design theory. For instance, Li et al. [49–52] analyzed the mechanism of negative stiffness and proposed a novel controllable negative-stiffness system using active control technology that can simultaneously achieve negative stiffness and controllable damping properties. Using control algorithms (LQR control, H_∞ control, and sliding mode control), a controllable system based on full-state feedback was created, which improved vibration control performance on all evaluation criteria. Walsh et al. [53, 54] proposed a displacement-based adjustable stiffness and energy dissipation (D-BASED) system that combined a resetting passive stiffness damper with a passive negative-stiffness device. An independent damper stiffness and energy dissipation can be designed for a D-BASED system. Compared to passive linear fluid viscous dampers, the D-BASED system produces smaller peak story drifts and foundation forces. Wang et al. [55, 56] proposed a novel track bistable nonlinear energy sink which exhibits negative stiffness to extend the energy range of the track energy sink and solved the energy-dependence issue that has arisen in conventional bistable nonlinear energy sinks. Iemura et al. [57–60] developed a magnetorheological fluid-based negative-stiffness damper to control structural dynamic responses, the effectiveness of which was demonstrated experimentally. Sun et al. [61, 62] proposed a negative stiffness friction damping device that can simultaneously provide negative stiffness and friction damping. Cimellaro et al. [63] proposed a three-dimensional base isolation system with a negative-stiffness device, which could reduce the vertical acceleration and the input energy transferred to the superstructure. Sarlis et al. [64–66] proposed a mechanism for amplifying negative stiffness. Both experimental tests and numerical simulations indicated that the displacement and acceleration responses can be controlled by a combination of negative stiffness and supplemental damping.

The major contribution of this paper is to propose a novel damping model with negative stiffness known as the half-cycle negative-stiffness damping model and to develop a corresponding device. An alternating transmission system and a one-way friction system are developed, which can be used to make a friction damping device to generate the half-cycle negative-stiffness damping model. The paper is organized as follows. Through analysis of a single degree of freedom (SDOF) system, Section 2 verifies that the half-cycle negative-stiffness damping model exhibits characteristics of negative stiffness. In addition, the equivalent expression of

the negative stiffness of the half-cycle negative-stiffness damping model is provided. Section 3 presents a half-cycle negative-stiffness damping device (HCNSDD) that consists of an alternating transmission system and a one-way friction system. In addition, a mechanical model of the HCNSDD is proposed. Section 4 describes experimental tests of the HCNSDD subjected to cyclic lateral loads to evaluate its hysteretic behavior and energy dissipation capacity. Finally, a finite element simulation approach for HCNSDD was presented, and the performance of seismic vibration control of HCNSDD was evaluated using a multidegree-of-freedom system.

2. Half-Cycle Negative-Stiffness Damping Model

2.1. The Mechanism of Half-Cycle Negative-Stiffness Damping Model. The half-cycle negative-stiffness damping model is transformed from the bilinear hysteretic damping model presented in Figure 1. The bilinear hysteretic [67–69] model is with hysteresis characteristics mainly related to intermittent contacts or elasto-plasticity, and it is observed in mechanical, civil, and aerospace. By eliminating the responses of the bilinear hysteretic damping model in the first and third quadrants, the half-cycle negative-stiffness damping mode is obtained, as shown in Figure 2. The half-cycle negative-stiffness damping mode exhibits an apparent negative stiffness (The slope of the F-x curve is negative, i.e., the stiffnesses of k_1, k_2, and k_3 are all less than 0 as illustrated in Figure 2).

The SDOF system with a supplemental damper is presented in Figure 3. In this figure, m, c, and k represent the mass, damping coefficient, and stiffness of the SDOF system, respectively. $F(x)$ is the supplemental damper. The excitation is denoted by P, $P = -ma\sin(\omega_i t + \theta_i)$. a, ω_i, t, and θ_i represent the excitation acceleration, excitation frequency, time, and phase angle, respectively. The equation of motion of the SDOF system with a supplemental damper is as follows:

$$m\ddot{x} + c\dot{x} + kx + F(x) = P. \tag{1}$$

Both sides of equation (1) are divided by k. If $y_s = ma/k$, $\omega_0 = \sqrt{k/m}$, and $\zeta_0 = c/2m\omega_0$, then equation (1) can be transformed into

$$\frac{1}{\omega_0^2}\ddot{x} + \frac{2\zeta_0}{\omega_0}\dot{x} + x + \frac{F(x)}{k} = -y_s\sin(\omega_i t + \theta_i). \tag{2}$$

The steady-state solution of equation (2) is assumed to be $x = b\sin\theta$ where $\theta = \omega_i t + \theta_i + \theta_0$, θ_0 is the phase angle, and b is the magnitude. If $\eta = \omega_i/\omega_0$, then equation (2) can be transformed into

$$-\eta^2\sin(\theta) + 2\zeta_0\eta\cos(\theta) + \sin(\theta) + \frac{F(x)}{kb} = -\frac{y_s}{b}\sin(\theta - \theta_0). \tag{3}$$

Both sides of equation (3) are multiplied by $\sin\theta$ and $\cos\theta$, respectively. According to trigonometric orthogonality, the result of one cycle $[\pi/2, 5\pi/2]$ is
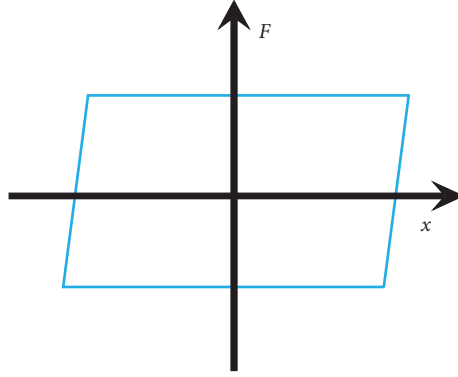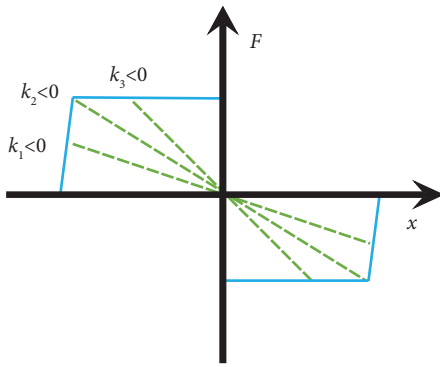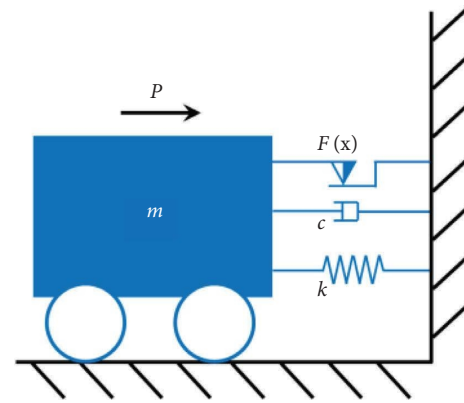
FIGURE 1: Bilinear hysteretic damping model. (Note: F is damping force, x is displacement).

FIGURE 2: Half-cycle negative-stiffness damping model. (Note: F is damping force, and x is displacement).

FIGURE 3: SDOF system.

$$\begin{cases} \eta^2 - 1 - \dfrac{1}{\pi k b} \displaystyle\int_{\pi/2}^{5\pi/2} F(\theta) \sin\theta d\theta = \dfrac{y_s}{b} \cos\theta_0, \\[4mm] 2\zeta_0\eta + \dfrac{1}{\pi k b} \displaystyle\int_{\pi/2}^{5\pi/2} F(\theta) \cos\theta d\theta = \dfrac{y_s}{b} \sin\theta_0. \end{cases} \tag{4}$$

Furthermore,

$$\left(\eta^2 - 1 - \dfrac{1}{\pi k b} \int_{\pi/2}^{5\pi/2} F(\theta) \sin\theta d\theta \right)^2 + \left(2\zeta_0\eta + \dfrac{1}{\pi k b} \int_{\pi/2}^{5\pi/2} F(\theta) \cos\theta d\theta \right)^2 = \left(\dfrac{y_s}{b} \right)^2. \tag{5}$$

The following subsections discuss the half-cycle negative-stiffness damping model and bilinear hysteretic damping model, respectively.

2.2. Half-Cycle Negative-Stiffness Damping Model. As depicted in Figure 4, for the half-cycle negative-stiffness damping model of one cycle $[\pi/2, 5\pi/2]$, the resistance force can be written as follows:
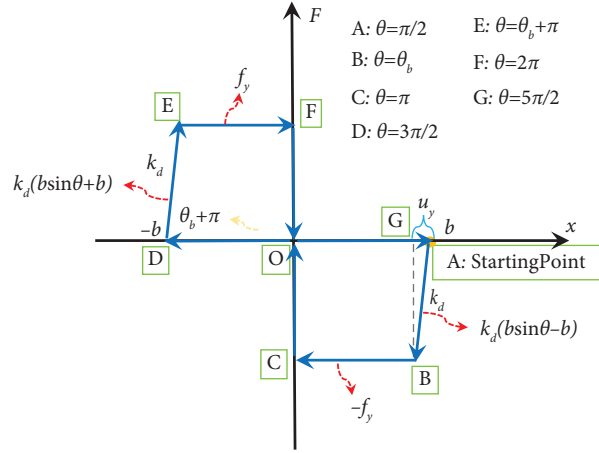
FIGURE 4: Half-cycle negative-stiffness damping model expression.

$$F(\theta) = \begin{cases} k_d\,(b\sin\theta - b), & [\pi/2, \theta_b], \\[2ex] -f_y, & (\theta_b, \pi], \\[2ex] 0, & \left(\pi, \dfrac{3\pi}{2}\right], \\[2ex] k_d\,(b\sin\theta + b), & \left(\dfrac{3\pi}{2}, \theta_b + \pi\right], \\[2ex] f_y, & (\theta_b + \pi, 2\pi], \\[2ex] 0, & \left(2\pi, \dfrac{5\pi}{2}\right], \end{cases} \qquad (6)$$

where f_y is the maximum damping force, $f_y = k_d u_y$. k_d is the stiffness of the half-cycle negative-stiffness damping model when the displacement is u_y. θ_b is the radian value of transition, formulated as $\theta_b = \pi - \arcsin(1 - u_y/b)$.

Substituting equations (6) into (5) to get the SDOF system with the half-cycle negative-stiffness damping model is

$$\left(\eta^2 - 1 - \left(\left(\frac{u_y}{b} - 1\right)\sqrt{\left(2 - \frac{u_y}{b}\right)\frac{u_y}{b}} - 2\frac{u_y}{b} + \arccos\left[1 - \frac{u_y}{b}\right]\right)\frac{k_d}{k\pi}\right)^2 + \left(2\zeta_0\eta + \frac{k_d}{k\pi}\left(2 - \frac{u_y}{b}\right)\frac{u_y}{b}\right)^2 = \left(\frac{y_s}{b}\right)^2. \qquad (7)$$

2.3. Bilinear Hysteretic Damping Model. As visualized in Figure 5, for the bilinear hysteretic damping model of one cycle $[\pi/2, 5\pi/2]$, the resistance force can be written as follows:
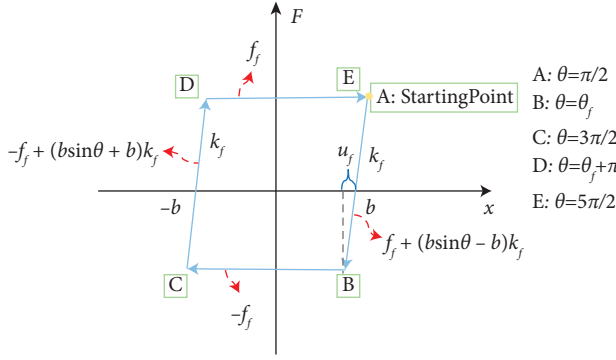
FIGURE 5: Bilinear hysteretic damping model expression.

where f_f is the maximum damping force, $f_f = k_f u_f$. k_f is the stiffness of the bilinear hysteretic damping when the displacement is u_f. θ_f is the radian value of transition, formulated as $\theta_f = \pi - arc\sin(1 - 2u_f/b)$

Substituting equations (8) into (5), the SDOF system with the bilinear hysteretic model is

$$
F(\theta) = \begin{cases}
f_f + (b\sin\theta - b)k_f, & \left[\pi/2, \theta_f\right], \\[2ex]
-f_f, & \left(\theta_f, \dfrac{3\pi}{2}\right], \\[2ex]
-f_f + (b\sin\theta + b)k_f, & \left(\dfrac{3\pi}{2}, \pi + \theta_f\right], \\[2ex]
f_f, & \left(\pi + \theta_f, \dfrac{5\pi}{2}\right],
\end{cases}
\tag{8}
$$

$$
\left(\frac{4k_f(b - u_f)u_f}{b^2\pi k} + 2\zeta_0\eta\right)^2
$$
$$
+ \left(-1 + \eta^2 - \frac{k_f}{k}\frac{\left(-2\sqrt{(b - u_f)u_f} + 4u_f\sqrt{((b - u_f)u_f/b^2)} + b\arccos\left[1 - (2u_f/b)\right]\right)}{b\pi}\right)^2 = \frac{y_s^2}{b^2}.
\tag{9}
$$

2.4. Mechanism Analysis of the Half-Cycle Negative-Stiffness Damping Model.

It is worth noting that when $u_y = 2 \times u_f$ and $k_d = k_f$ (i.e., the maximum damping force f_y for the half-cycle negative-stiffness damping model is twice the maximum damping force f_f for the bilinear hysteretic damping model), the energy dissipation of the two damping models is nearly identical in one cyclic of loading at a given displacement magnitude. With this, the difference in the frequency response function obtained by comparing the two types of damping models is due to the difference in the shape of damping model. In addition, u_y and u_f should be set with much smaller values compared to the loading displacement of the model (less than 1/20 of the loading displacement magnitude of the model), for ensuring the model can reasonably present Coulomb damping. Assuming $u_f = 0.0125$ dm, $u_y = 0.025$ dm, $k_d = k_f = [3, 5, 7]$ N/dm, and $\zeta_0 = 0.05$, $k = 1$ N/dm, $y_s = 0.5$ dm. From equation (7), the relationship between displacement response coefficient (b/y_s) and η of the half-cycle negative-stiffness damping model is obtained, as presented in Figure 6(a). From equation (9),

the relationship between displacement response coefficient and η of the bilinear hysteretic damping model is obtained, as depicted in Figure 6(b).

Figure 6(a) demonstrates that the displacement response coefficient of SDOF system decreases as k_d increases (i.e., the half-cycle negative-stiffness damping model force f_y increases). Compared with the uncontrolled SDOF system, the addition of the half-cycle negative-stiffness damping model decreases the peak value of frequency response by 9.04%, 15.04%, and 21.20% for $k_d = 3$, 5 and 7 N/dm, respectively. In addition, the resonance frequency ω_i of SDOF system decreases as k_d increases. This indicates that the half-cycle negative-stiffness damping model can reduce the entire stiffness of the system. Therefore, the half-cycle negative-stiffness damping model exhibits negative stiffness characteristics. Figure 6(b) demonstrates that the displacement response coefficient of the SDOF system decreases as k_f increases (i.e., the bilinear hysteretic damping model f_f increases). Compared with the uncontrolled SDOF system, the bilinear hysteretic damping model decreased by 9.53%,
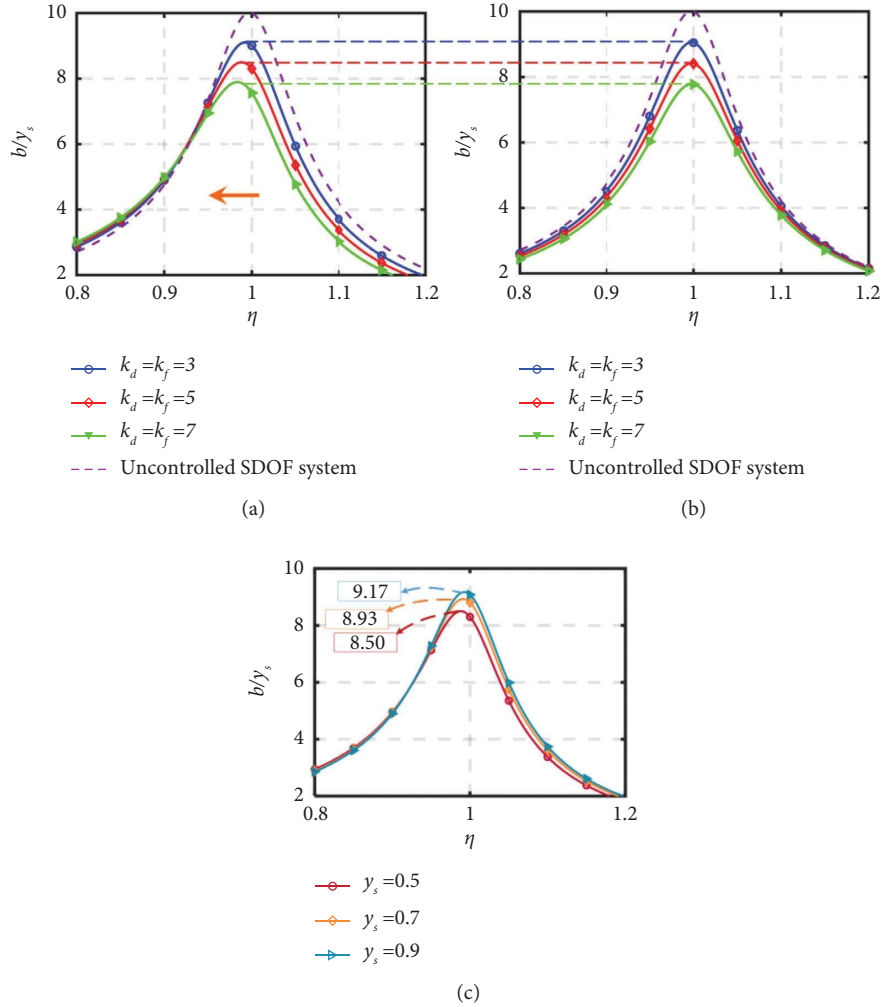
(a)

(b)

(c)

FIGURE 6: Relationship between displacement response coefficient (b/y_s) and η: (a) half-cycle negative-stiffness damping, (b) bilinear hysteresis damping, and (c) displacement response coefficient of half-cycle negative-stiffness damping ($k_d = 5$) under different magnitudes of excitation.

15.87%, and 22.22% for $k_f = 3$, 5, and 7 N/dm, respectively. However, the resonance frequency of SDOF system remained the same. Figure 6(c) indicates that the displacement response coefficient of the SDOF system with half-cycle negative-stiffness damping varies under different magnitudes of excitation ($y_s = [0.5, 0.7, 0.9]$ dm), particularly for the near resonant frequency. Such variation is related to the nonlinear effect on the half-cycle negative-stiffness damping.

As the above description suggests, the two damping models exhibit similar control of the displacement response coefficient when the energy dissipation is the same. However, the half-cycle negative-stiffness damping model reduces the resonance frequency by adding negative stiffness.

2.5. Equivalent Parameters of the Half-Cycle Negative-Stiffness Damping Model

2.5.1. Equivalent Negative-Stiffness. Section 2.4 demonstrated that the half-cycle negative-stiffness damping model

is a damping model with negative stiffness characteristics. In this section, the equivalent negative stiffness of the half-cycle negative-stiffness damping model is investigated.

Transforming equation (7) in Taylor expansion and assuming $\zeta_0 = 0$ yield

$$\left(\eta^2 - 1 + 2\frac{k_d u_y}{kb\pi}\right)^2 + \left(\frac{k_d u_y}{kb\pi}\left(2 - \frac{u_y}{b}\right)\right)^2 = \left(\frac{y_s}{b}\right)^2. \quad (10)$$

Set

$$F(\eta, b) = \left(\eta^2 - 1 + 2\frac{k_d u_y}{k\pi b}\right)^2 + \left(\frac{k_d u_y}{k\pi b}\left(2 - \frac{u_y}{b}\right)\right)^2 - \left(\frac{y_s}{b}\right)^2 = 0. \quad (11)$$

The following equation can be obtained from equation (11):

$$\frac{\partial b}{\partial \eta} = -\frac{(\partial F/\partial \eta)}{(\partial F/\partial b)} = -\frac{4\eta\left(\eta^2 - 1 + 2\left(k_d u_y/k\pi b\right)\right)}{(\partial F/\partial b)}. \quad (12)$$

With equation (12) = 0, the resonance of the SDOF system can be calculated by

$$4\eta\left(\eta^2 - 1 + 2\frac{k_d u_y}{k\pi b}\right) = 0. \quad (13)$$

Substituting $\eta = \omega_i/\omega_0$, $\omega_0 = \sqrt{k/m}$, $f_y = k_d u_y$ into equation (13) to obtain k_h (the stiffness of the SDOF system with the half-cycle negative-stiffness damping model) gives

$$k_h = k - \frac{2f_y}{\pi b}. \quad (14)$$

Therefore, the equivalent negative-stiffness k_{eh} of the half-cycle negative-stiffness damping model is

$$k_{eh} = -\frac{2f_y}{\pi b}. \quad (15)$$

Using equation (15), the equivalent negative stiffness of the half-cycle negative-stiffness damping model is proportional to f_y and inversely affected by b. Therefore, the frequency decreases as k_d becomes larger, as shown in Figure 6(a). For the same value of b, the larger the force f_y is (i.e., k_d becomes larger), the larger equivalent negative stiffness is obtained.

2.5.2. Equivalent Viscous Damping Constant. Based on the equivalent principle of equal relative displacement and equal hysteresis energy between the half-cycle negative-stiffness damping and the viscous damping under the premise of resonance [70], as shown in Figure 7, the equivalent viscous damping constant of the half-cycle negative-stiffness damping is

$$E = c_{eh}\omega_i\pi b^2 = 2bf_y, \quad (16)$$

where E is hysteresis energy; c_{eh} is the equivalent viscous damping constant of the half-cycle negative-stiffness damping.
Furthermore,

$$c_{eh} = \frac{2f_y}{\omega_i\pi b}. \quad (17)$$

3. Mechanism and Mechanical Model of the HCNSDD

As demonstrated in Figure 8, a half-cycle negative-stiffness damping model can be regarded as a bilinear hysteretic damping model (i.e., friction damping model) by eliminating the first and third quadrants; hence, friction damping only exists in the unloading stage. To realize the mechanism, the alternating transmission system and the one-way friction system are proposed.

3.1. One-Way Friction System. The one-way friction system is composed of a one-way bearing, friction ring, connecting rod, and friction plates, as illustrated in Figure 9. The A-end of the connecting rod is fixed to the inner ring of the one-
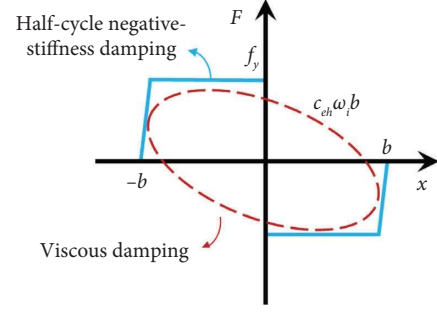
Figure 7: Equivalence between the half-cycle negative-stiffness damping and viscous damping.
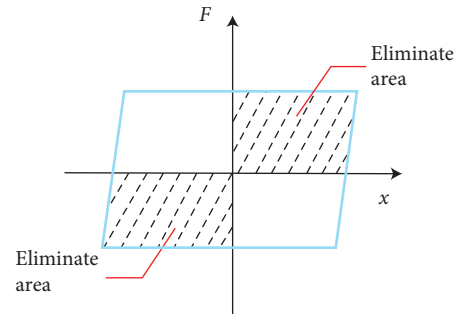
Figure 8: Generation mechanism of the half-cycle negative-stiffness damping model.

way bearing. The outer ring of the one-way bearing is fixed with a friction ring, and both sides of the friction ring are pressured by the friction plate with the pressure force N. When the connecting rod causes the one-way bearing to rotate, the one-way bearing drives the friction ring to generate friction damping force.

The one-way bearing has a one-way rotation function, similar to a ratchet. The inner and outer rings can rotate freely in one direction. In the other direction, the inner and outer rings are locked to transmit torque. A photograph of the one-way bearing is presented in Figure 10.

The B-end of the connecting rod is fixed in the gears of the alternating transmission system. The friction damping in the first and third quadrants can be eliminated by free rotating in the direction of the one-way bearing.

3.2. Alternating Transmission System. The alternating transmission system is composed of a nonfull rack and gears, as depicted in Figure 11. The gears are arranged at both ends of the nonfull rack. They are fixed, and the rack can move horizontally. The rack and gear [15, 71, 72] mechanism transforms relative translational motion at both ends of the device into rotational motion. When the rack is moved to either side, it meshes only one side of the gear. As illustrated in Figure 11(b), when the rack moves from the initial stage to the right, it meshes with the right gear, making the right gear rotate counterclockwise, as indicated by the red arrow. In addition, when the rack moves from right to left, the right gear is made to rotate clockwise, as indicated by the green
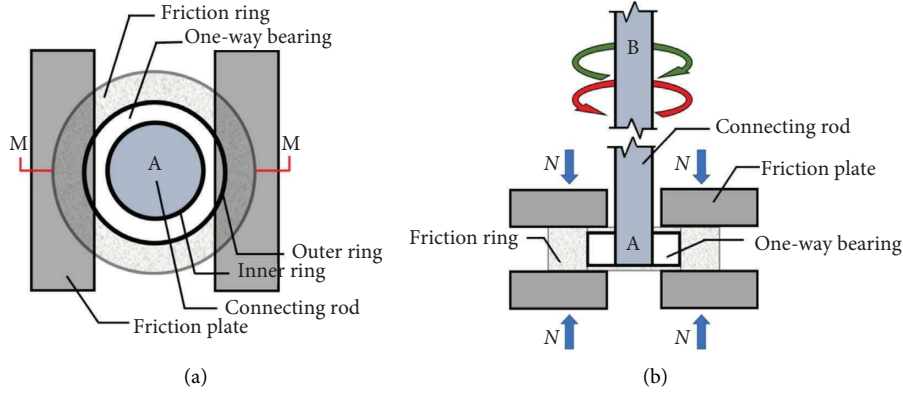
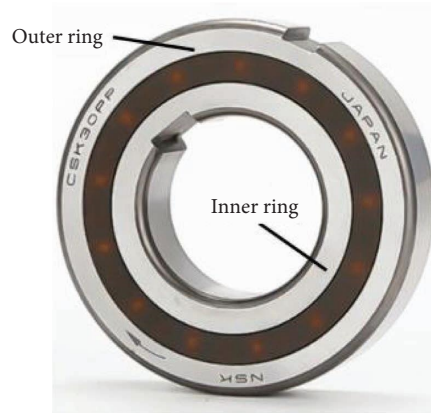FIGURE 9: One-way friction system: (a) top view and (b) M-elevation view.

FIGURE 10: Photograph of the one-way bearing.

arrow. Similarly, as depicted in Figure 11(c), when the rack meshes with the left gear, it makes the left gear rotate counterclockwise and clockwise, as indicated by the green and red arrows, respectively.

The alternating transmission system makes the right gear generate friction damping in the first and fourth quadrants (i.e., Figures 11(b) and 11(c)), while the left gear generates frictional damping in the second and third quadrants.

3.3. The Mechanism of the HCNSDD. As illustrated in Figure 12, the alternating transmission system and the one-way friction system are assembled to develop the HCNSDD. Two ends of the HCNSDD have connecting devices-I and II. The transmission rod is connected with the connecting device-I and passes through the linear bearings of HCNSDD. A rack is fixed in the middle of the transmission rod. This can drive the rack to generate horizontal displacement. Gears are placed on each side of the rack, as depicted in Figure 12(a). When the HCNSDD is loaded in any direction, the rack only meshes with the gear on one side. As Figure 12(b) illustrates, two sides of the connecting rod are connected to the gear and the inner ring of the one-way bearings, respectively. The outer ring of the one-way bearing is fixed to the friction ring. The red arrow direction indicates free rotation in the

direction of the one-way bearing, while the green arrow is the locking direction of the one-way bearing, as presented in Figure 12(a). Friction plates are fixed on one side of pressure plates-I and II. Using bolts, the friction plates press the friction ring. Figure 12(c) is a three-dimensional model of the HCNSDD, where the red dotted line refers to the zoomed-in view of the one-way friction system.

Under one cycle of loading, the hysteretic curve depicted in Figure 13 can be generated, the process for which is as follows:

(1) Loading I: The rack meshes with the right side of the gear to generate rotation. The gear drives the one-way bearing to rotate through the connecting rod. The inner and outer rings of the one-way bearing are free to rotate in this direction. Therefore, the friction ring does not generate friction damping in loading I stage (i.e., the first quadrant).

(2) Unloading I: The rack drives the right gear to rotate counterclockwise. The inner and outer rings of the one-way bearing in this direction are locked, and the friction ring is driven to rotate through the connecting rod. Therefore, the friction ring rotates to generate friction damping in unloading I stage (i.e., the fourth quadrant).
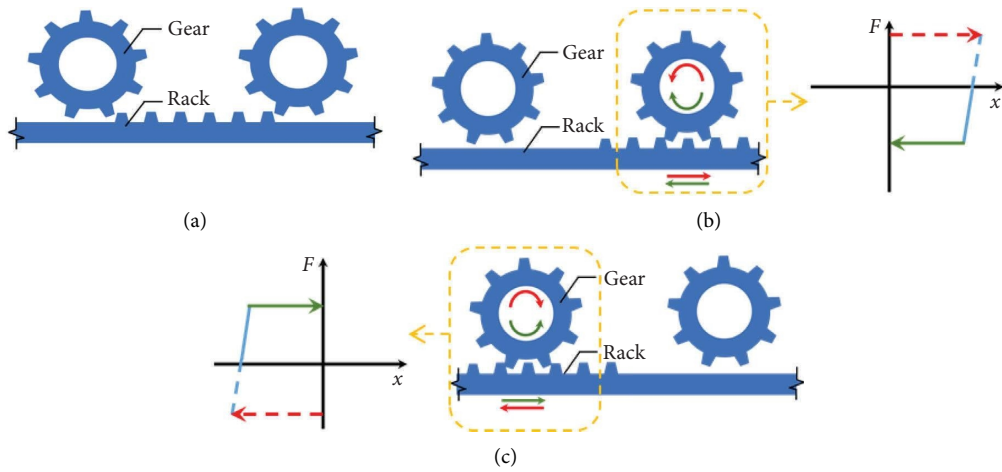
FIGURE 11: Mechanism of the alternating transmission system: (a) initial state, (b) rack meshes with the right gear, and (c) rack meshes with the left gear.
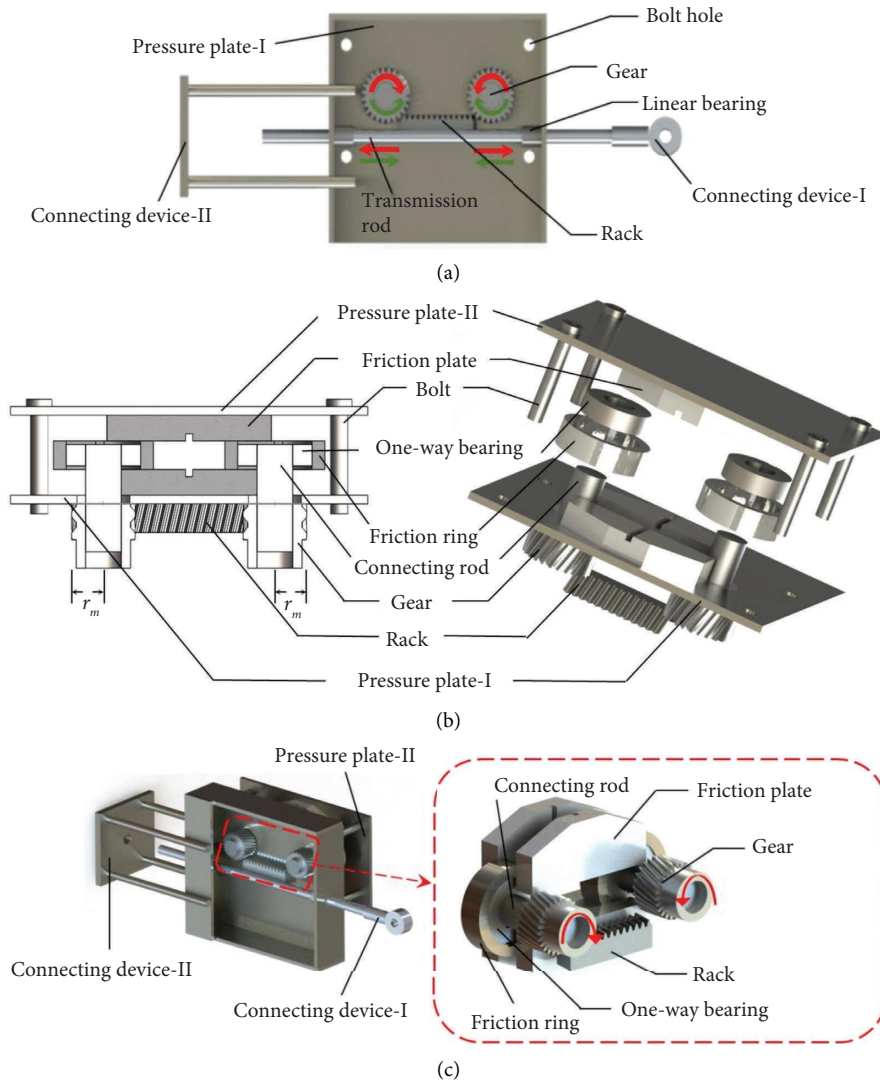

FIGURE 12: Mechanism of the HCNSDD: (a) schematic diagram of the alternating transmission system (red arrow: rotating freely does not generate friction damping. green arrow: rotating that is locked generates friction damping), (b) schematic diagram of the one-way friction system, and (c) three-dimensional model of the HCNSDD.
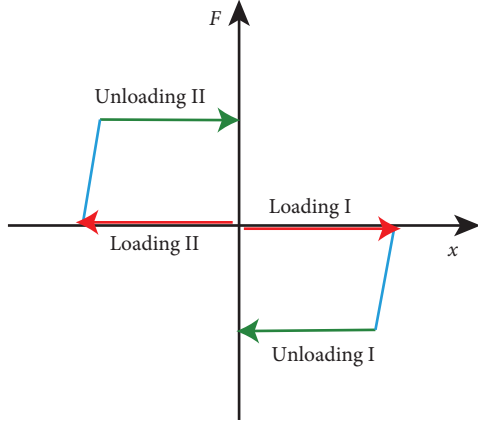
FIGURE 13: Hysteretic curve generated by the HCNSDD.

(3) Loading II: The rack is separated from the right gear and meshes with the left gear. The inner and outer rings of the one-way bearing are free to rotate in this direction. Similarly, the friction ring does not generate friction damping in loading II stage (i.e., the third quadrant).

(4) Unloading II: The rack drives the left gear to rotate counterclockwise. The inner and outer rings of the one-way bearing in this direction are locked. Similarly, the friction ring rotates to generate friction damping in unloading II stage (i.e., the second quadrant).

3.4. Mechanical Model. The mechanism of the HCNSDD indicates that the pressure force is generated by the bolts. Assuming that the pressure force on the friction ring is uniformly distributed, and the pressured area of the friction ring is S, then the intensity of pressure p generated by the bolt can be expressed as

$$p = \frac{nM_b}{KSd_b}, \tag{18}$$

where d_b is the diameter of the bolt, M_b is the torque of the bolt, n is the number of bolts, and K is the torque coefficient.

As illustrated in Figure 14, assuming the pressured friction ring is a microring with a radius of r. The thickness of the microring is dr. The pressured area dA of microring by the friction plate can be obtained by

$$dA = 2\pi erdr, \tag{19}$$

where e is the radian ratio of the pressured friction ring to the entire friction ring.

The torque dT_f generated by the microring is

$$dT_f = 2P\mu rdA. \tag{20}$$

Furthermore, the expression of the torque T_f generated by the friction ring is

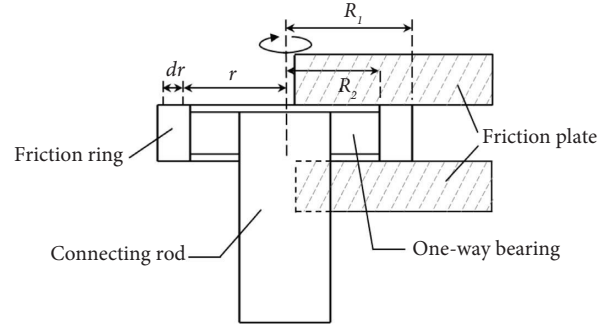$$T_f = 4\int_{R_2}^{R_1} \pi P\mu er^2 dr, \tag{21}$$

FIGURE 14: Schematic diagram of the microring of the friction ring.

where μ is the friction coefficient between the friction ring and the friction plate, R_1 is the outer radius of the friction ring, and R_2 is the inner radius of the friction ring.

Substituting equation (21) into $T_f = F \cdot r_m$ where r_m is the dividing circle radius of the gear (see Figure 12(b)). The transitions between the loading and unloading stages are assumed to be instantaneous. The mechanical model for the restoring force F_h of the HCNSDD can be transformed into

$$F_h = \begin{cases} 0, & \text{Loading stage,} \\ \\ \text{sgn}(\dot{x}) \dfrac{4}{r_m} \displaystyle\int_{R_2}^{R_1} \pi P\mu er^2 dr, & \text{Unloading stage,} \end{cases} \tag{22}$$

where $\dot{x}$ is the velocity of the device.

4. HCNSDD Experiments

4.1. Experimental Specimen. The HCNSDD specimen was made of Q345b steel. The pressure plate was pressed with four bolts. The main parameters of the HCNSDD are presented in Table 1. The experimental specimen of the HCNSDD is depicted in Figure 15. The specimen was loaded by an axial loading facility. The loading facility utilizes PID control method to load the HCNSDD for sinusoidal displacement loading. A load cell was installed in the end of the connecting device-II to measure the force of the HCNSDD. The loading facility to load the HCNSDD with the loading displacement magnitude (i.e., Δ) of 30 and 50 mm, respectively, and a frequency of 0.05 Hz with a sinusoidal excitation was applied.

4.2. Experimental Results. The effect of the pressure force applied by the bolts and the loading displacement magnitude on the cyclic behavior of HCNSDD was investigated in this experiment. The torque applied to the bolts (i.e., M_b) was 5, 7.5, and 10 N·m, which resulted in pressure forces of 4463 N, 6448 N, and 8886 N, respectively. Two displacement magnitudes for the sinusoidal loading were considered, i.e., 30 and 50 mm. Note that the displacement magnitude of 50 mm was governed by the displacement capacity of the loading facility, while the actual stroke limit of the experimental HCNSDD device was 62 mm.

TABLE 1: Main parameters of the HCNSDD.

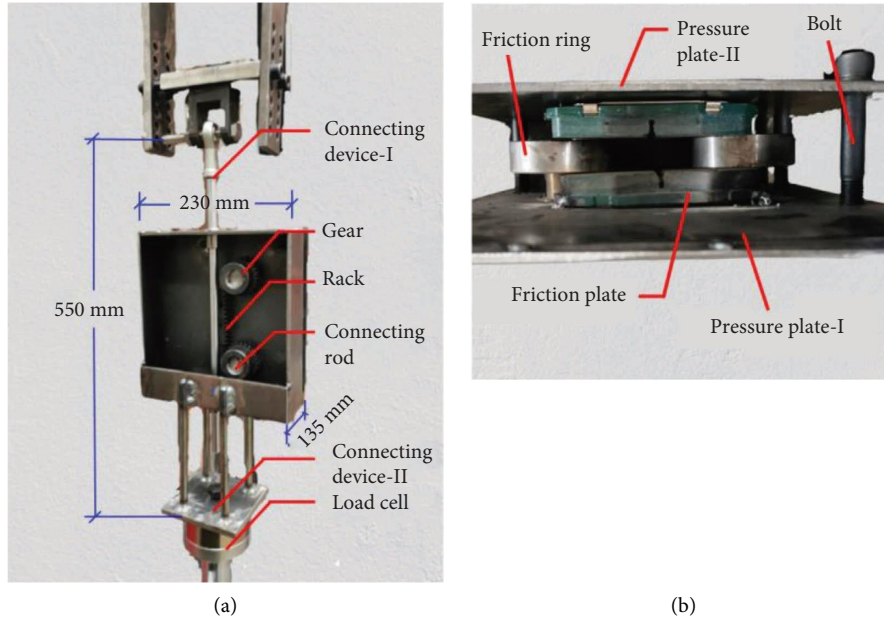| Parameters	Values
e	0.2
d	12 mm
r_m	24
R_1/R_2	35 mm/26 mm
μ	0.35
K	0.282

(a)

(b)

FIGURE 15: Experimental specimen of the HCNSDD: (a) front view and (b) side view.

A comparison between the experimental results and theoretical results (from equation (22)) is presented in Figure 16. This indicates that the alternating transmission system and the one-way friction system eliminate friction in the loading stage. In this way, the purpose of generating friction only in the unloading stage is achieved. The HCNSDD can generate a half-cycle negative-stiffness damping model with stable hysteretic curves. It is important to note that the damping forces in the fourth quadrant of Figures 16(c) and 16(d) were slightly lower than the theoretical results. This was caused by the uneven pressure applied by four bolts, which would slightly influence the friction forces in the experiments.

Figure 17 indicates that the maximum friction force is proportional to the torque of bolts (i.e., the pressure force applied by the bolts). The average discrepancy between the theoretical and experimental values of the damping force of the H-CNSDD is less than 6%. Such discrepancy is majorly due to the uneven pressure forces applied by four bolts.

Figure 18 indicates that the equivalent stiffness value (from equation (15)) of the HCNSDD is proportional to the torque of the bolt, while the displacement magnitude inversely impacts it. During the experiments, the gears and rack worked stably and exhibited good robustness. The

experiments indicated that a device that can generate the half-cycle negative-stiffness damping model has been successfully developed.

5. Finite Element Analysis of the HCNSDD

5.1. Modeling of the HCNSDD in SAP2000.
The HCNSDD can be readily implemented in the program SAP2000 using two elements in parallel. As shown in Figure 19, a Wen plastic element and a multilinear elastic element are defined, and the summarization of hysteretic curves of the two elements results in a reasonable reproduction of the HCNSDD hysteretic behavior.

5.2. Analytical System.
The following assumptions are made in the design and analysis of the multidegree-of-freedom (MDOF) system: (1) the mass of each story is the same, (2) the height of each story is the same, and (3) no yielding occurs in the MDOF system.

The idealization of a five-story shear-type building can be represented by a MDOF system. The mass of each floor, the stiffness of each story, and the height of each story are $m_s = 5 \times 10^5$ kg, $k_s = 9 \times 10^5$ kN/m, and $h_s = 3$ m, respectively (as shown in Figure 20). The natural period is 0.53 s. The
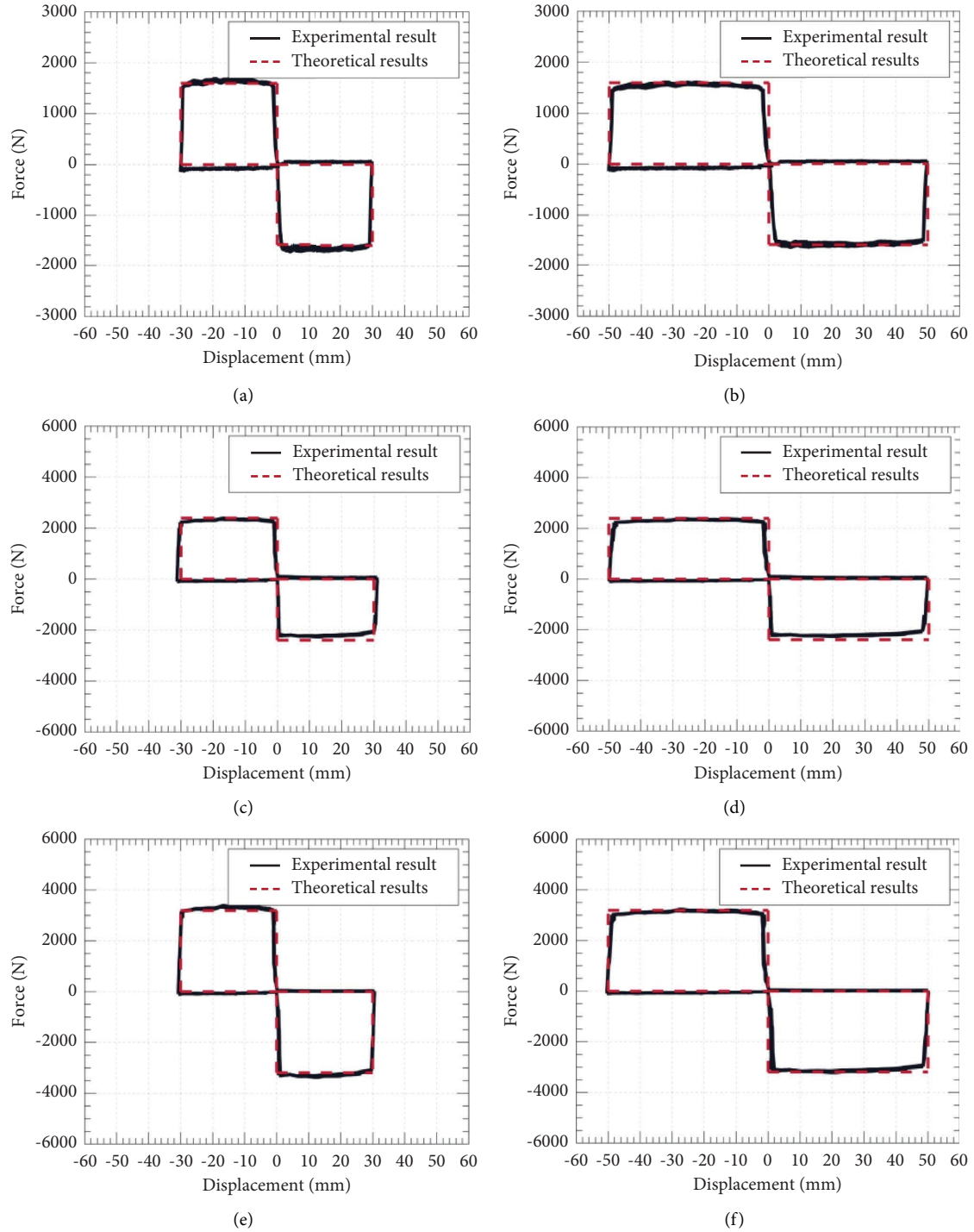
FIGURE 16: Comparison of experimental results and theoretical results of the HCNSDD: (a) ($M_b = 5$ N·m), $\Delta = 30$ mm; (b) ($M_b = 5$ N·m), $\Delta = 50$ mm; (c) ($M_b = 7.5$ N·m), $\Delta = 30$ mm; (d) ($M_b = 7.5$ N·m), $\Delta = 50$ mm; (e) ($M_b = 10$ N·m), $\Delta = 30$ mm; (f) ($M_b = 10$ N·m), $\Delta = 50$ mm.

damping ratio of each mode is assumed to be 3%. The structure is incorporated with one HCNSDD in each story, and each HCNSDD can provide a damping force of 8×10^6 N. Three seismic motions, the El-Centro (1940), Kobe (1995), and Chi-Chi (1999), are selected for the simulation input seismic motions, and the seismic motions are scaled to 0.4 g [73].

5.3. Simulation Results. Figure 21 compares the input energy to the uncontrolled structure and HCNSDD-controlled structure when subjected to three seismic motions. Compared with the uncontrolled structure, the seismic input energy of the HCNSDD-controlled structure is significantly reduced by 56.3%, 60.4%, and 50.1%, for the El-Centro, Kobe, and Chi-Chi motions, respectively. Such decrease in
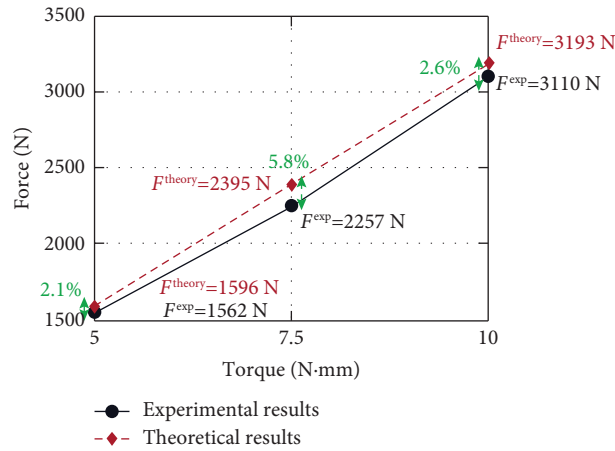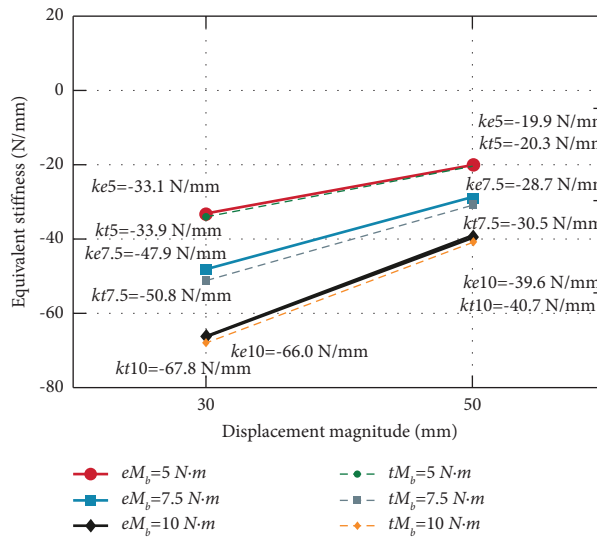
FIGURE 17: Average damping force of the HCNSDD.

FIGURE 18: Equivalent negative stiffness of the HCNSDD (Note: e denotes the experimental results, t denotes the theoretical results, and numbers denotes the torque).
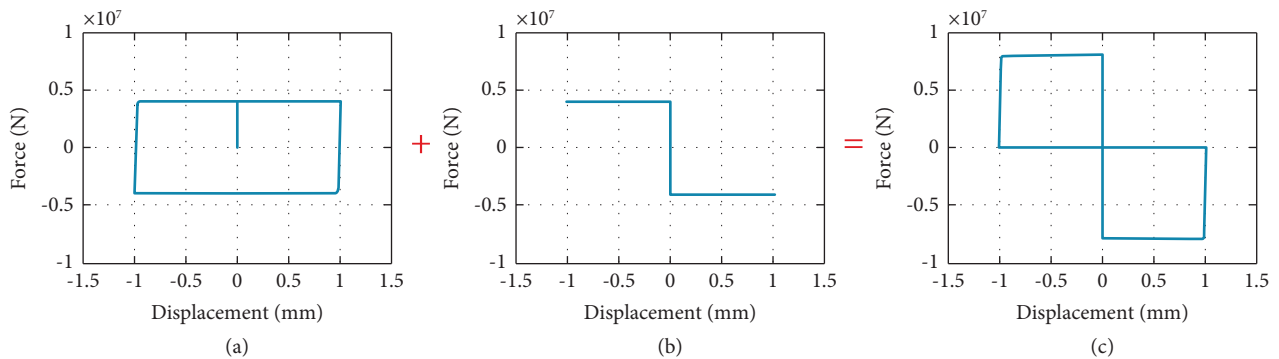

FIGURE 19: The HCNSDD simulation in SPA2000: (a) Wen plastic element, (b) multilinear elastic element, and (c) HCNSDD.

the seismic input energy [58] is because of the negative stiffness provided by the additional HCNSDD of the system.

Figure 22 shows the change in the interstory drift ratio of the structure under different seismic motions. Although the HCNSDD has negative stiffness, the HCNSDD provides large damping which effectively controls the deformation response of the structure. Compared with the uncontrolled structure, the average interstory drift ratio of the HCNSDD-controlled structure is reduced by 44.70% under the three seismic motions, and the reduction ratio of each story is shown in Figure 22.
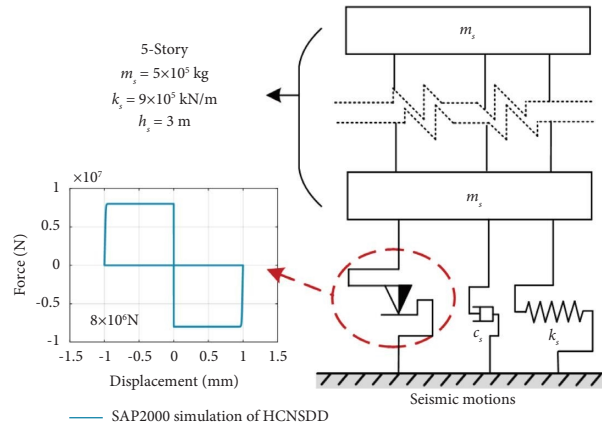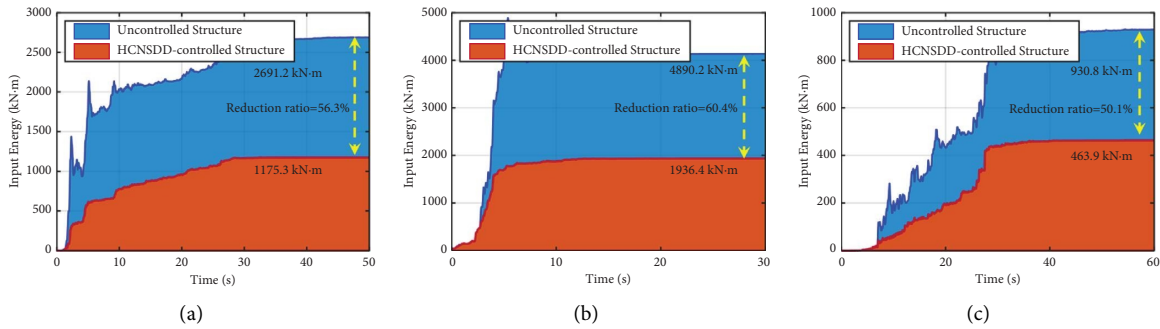
FIGURE 20: HCNSDD-controlled structure.

FIGURE 21: Input energy under different seismic motions. (Reduction ratio = (uncontrolled structure – HCNSDD-controlled structure)/ uncontrolled structure). (a) El-Centro, (b) Kobe, and (c) Chi-Chi.
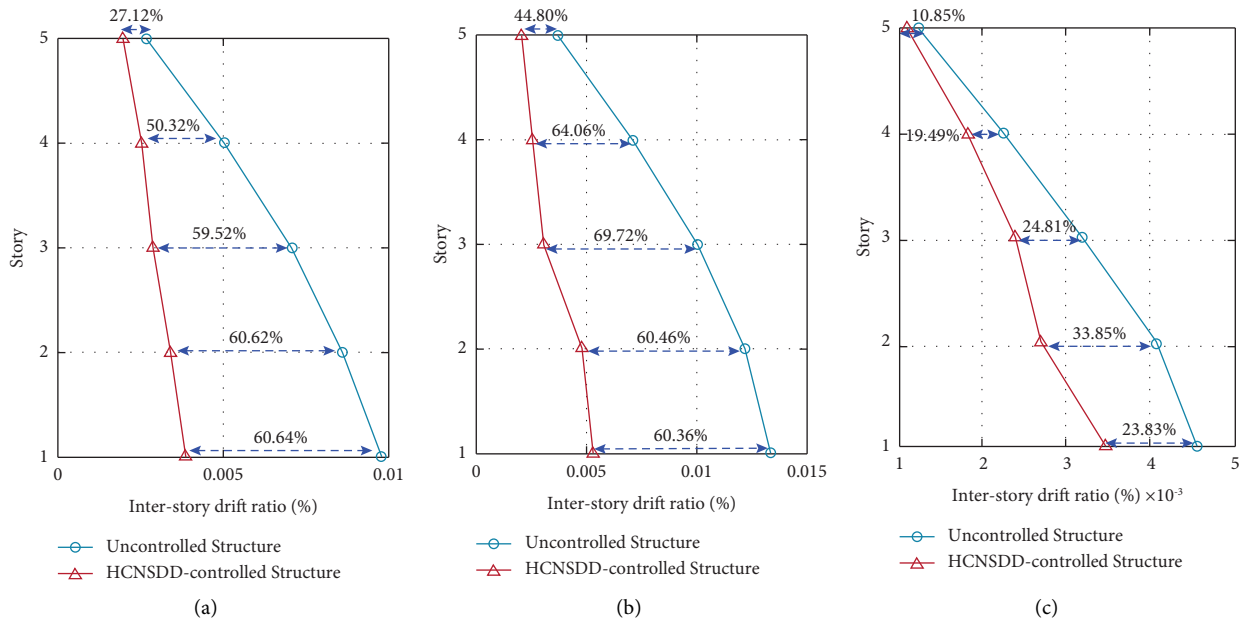

FIGURE 22: Interstory drift ratio under different seismic motions: (a) El-Centro, (b) Kobe, and (c) Chi-Chi.
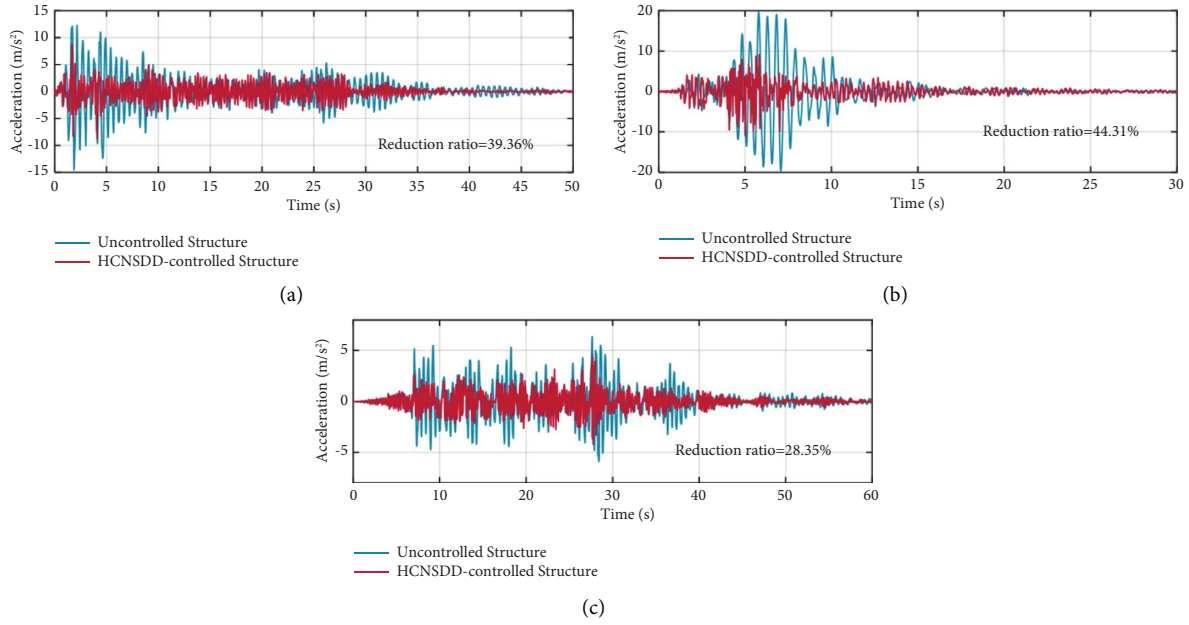
FIGURE 23: Acceleration time history under different seismic motions. (a) El-Centro, (b) Kobe, and (c) Chi-Chi.

Figure 23 shows the acceleration time history response of the structure under different seismic motions. It can be seen that the HCNSDD can effectively reduce the acceleration response. Compared with the uncontrolled structure, the peak acceleration response of the HCNSDD-controlled structure is significantly reduced by 39.36%, 44.31%, and 28.35%, for the El-Centro, Kobe, and Chi-Chi motions, respectively.

6. Conclusions

In this paper, a novel damping model with negative stiffness was proposed, and a half-cycle negative-stiffness damping device (HCNSDD) was developed. The following conclusions can be drawn from this study.

(1) Analysis of the single degree of freedom (SDOF) system demonstrated that the half-cycle negative-stiffness damping model can reduce the displacement response and decrease the natural vibration frequency of the SDOF system. This indicates that the proposed half-cycle negative-stiffness damping model has negative stiffness characteristics. The equivalent expression of the half-cycle negative-stiffness damping model was derived, and the finite element simulation approach for HCNSDD was presented.

(2) A device of the HCNSDD was proposed, which comprised the alternating transmission system and the one-way friction system. By arranging two systems, the HCNSDD was able to generate the half-cycle negative-stiffness damping model. A mechanical model was developed to represent the force-displacement relationship of the proposed HCNSDD.

(3) Experimental tests of the HCNSDD subjected to cyclic loads were conducted to examine its hysteretic behavior. The HCNSDD specimen exhibited a clear half-cycle negative-stiffness damping model and stable energy dissipation, verifying the effectiveness of the proposed HCNSDD.

Nomenclature

m: Mass of SDOF system
k: Stiffness of SDOF system
F: Damping force
x: Displacement
c: Damping coefficient of SDOF system
d: Supplemental damper
P: Excitation force
a: Excitation acceleration
ω_i: Excitation frequency
t: Time
θ_i, θ_0: Phase angle
b: Magnitude of dynamic displacement response
$\omega_0 = \sqrt{k/m}$: Natural frequency of SDOF system
$\zeta_0 = c/2m\omega_0$: Damping ratio of SDOF system
$\eta = \omega_i/\omega_0$: Ratio of excitation frequency to natural frequency of the SDOF system
$y_s = ma/k$: Static displacement response of the SDOF system
k_d: Stiffness of the half-cycle negative-stiffness damping model when the displacement is u_y
f_y: Maximum damping force of the half-cycle negative-stiffness damping model
θ_b: Radian value of transition of the half-cycle negative-stiffness damping model

f_f:	Maximum damping force of the bilinear hysteresis damping model
k_f:	Stiffness of the bilinear hysteresis damping model when the displacement is u_y
θ_f:	Radian value of transition of the bilinear hysteresis damping model
k_h:	Stiffness of the SDOF system with the half-cycle negative-stiffness damping model
k_{eh}:	Equivalent negative stiffness of the half-cycle negative-stiffness damping model
E:	Hysteresis energy
c_{eh}:	Equivalent viscous damping constant of the half-cycle negative-stiffness damping
N:	Pressure force
p:	Intensity of pressure generated by the bolts
S:	Pressured area of the friction ring
d_b:	Diameter of the bolt
M_b:	Torque of bolt
n:	Number of bolts
K:	Torque coefficient
r:	Radius of microring
dr:	Thickness of the microring
dA:	Area of the microring
e:	Radian ratio of the pressured friction ring to the entire friction ring
dT_f:	Torque of the microring
T_f:	Torque of the friction ring
μ:	Friction coefficient
R_1:	Outer radius of the friction ring
R_2:	Inner radius of the friction ring
F_h:	Mechanical model of the HCNSDD
r_m:	Dividing circle radius of the gear
Δ:	Loading displacement magnitude
$\dot{x}$:	Velocity of the HCNSDD
m_s:	Mass of each story
k_s:	Stiffness of each story
h_s:	Height of each story.

Data Availability

The data that support the findings of this study are available from the corresponding author upon reasonable request.

Conflicts of Interest

All authors declare that there are no conflicts of interest.

Acknowledgments

References

[1] J. Y. Shang, P. Tan, Y. F. Zhang, J. P. Han, and J. J. Qin, "Experimental and analytical investigation of variable friction pendulum isolator," *Engineering Structures*, vol. 243, Article ID 112575, 2021.

[2] K. Ikago, K. Saito, and N. Inoue, "Seismic control of single-degree-of-freedom structure using tuned viscous mass damper," *Earthquake Engineering and Structural Dynamics*, vol. 41, no. 3, pp. 453–474, 2012.

[3] X. D. Ji, Y. H. Cheng, and C. Molina Hutt, "Seismic response of a tuned viscous mass damper (TVMD) coupled wall system," *Engineering Structures*, vol. 225, Article ID 111252, 2020.

[4] X. D. Ji, J. S. Zhang, K. Ikago, S. Chakraborty, and H. Kanno, "Tuned viscous mass damper (TVMD) coupled wall system for enhancing seismic performance of high-rise buildings," *Engineering Structures*, vol. 240, Article ID 112307, 2021.

[5] Y. H. Cheng, X. D. Ji, K. Ikago, and H. Luo, "Analytical solutions of H_2 control and efficiency-based designs of structure systems equipped with a tuned viscous mass damper," *Structural Control and Health Monitoring*, vol. 29, no. 5, Article ID e2932, 2022.

[6] X. Ji, X. Gao, Y. Zhuang, and Z. Qu, "Enhanced measurements of structural inter-story drift responses in shaking table tests," *Engineering Structures*, vol. 278, Article ID 115508, 2023.

[7] Y. H. Cheng and X. D. Ji, "Robustness of a tuned viscous mass damper (TVMD) controlled system," *Advances in Structural Engineering*, vol. 25, no. 16, pp. 3349–3367, 2022.

[8] X. D. Ji, T. Hikino, K. Kasai, and M. Nakashima, "Damping identification of a full-scale passively controlled five-story steel building structure," *Earthquake Engineering and Structural Dynamics*, vol. 42, no. 2, pp. 277–295, 2013.

[9] Z. Lai, T. Sun, and S. Nagarajaiah, "Adjustable template stiffness device and SDOF nonlinear frequency response," *Nonlinear Dynamics*, vol. 96, no. 2, pp. 1559–1573, 2019.

[10] A. A. Sarlis, D. T. R. Pasala, M. C. Constantinou, A. M. Reinhorn, S. Nagarajaiah, and D. P. Taylor, "Negative stiffness device for seismic protection of structures," *Journal of Structural Engineering*, vol. 139, no. 7, pp. 1124–1133, 2013.

[11] T. R. Giri and R. Mailen, "Controlled snapping sequence and energy absorption in multistable mechanical metamaterial cylinders," *International Journal of Mechanical Sciences*, vol. 204, Article ID 106541, 2021.

[12] Y. Zhang, S. Wang, H. Fang, H. Han, and Y. Xu, "Design and simulation of a damper with negative stiffness for vibration mitigation from drilling equipment to a semi-submersible platform," *Shock and Vibration*, vol. 2020, Article ID 2605381, 15 pages, 2020.

[13] S. Yuan, Y. Sun, M. Wang et al., "Tunable negative stiffness spring using Maxwell normal stress," *International Journal of Mechanical Sciences*, vol. 193, Article ID 106127, 2021.

[14] M. H. Pradono, H. Iemura, A. Igarashi, A. Toyooka, and A. Kalantari, "Passively controlled MR damper in the benchmark structural control problem for seismically excited highway bridge," *Structural Control and Health Monitoring*, vol. 16, no. 6, pp. 626–638, 2009.

[15] D. Pietrosanti, M. De Angelis, and A. Giaralis, "Experimental seismic performance assessment and numerical modelling of nonlinear inerter vibration absorber (IVA)-equipped base isolated structures tested on shaking table," *Earthquake Engineering and Structural Dynamics*, vol. 50, no. 10, pp. 2732–2753, 2021.

[16] M. C. Smith, "Synthesis of mechanical networks: the inerter," *IEEE Transactions on Automatic Control*, vol. 47, no. 10, pp. 1648–1662, 2002.

[17] M. C. Smith, "The inerter: a retrospective," *Annual Review of Control, Robotics, and Autonomous Systems*, vol. 3, no. 1, pp. 361–391, 2020.

[18] H. Garrido, O. Curadelli, and D. Ambrosini, "Resettable-inertance inerter: a semiactive control device for energy absorption," *Structural Control and Health Monitoring*, vol. 26, no. 11, p. e2415, 2019.

[19] A. D. Shaw, G. Gatti, P. J. P. Gonçalves, B. Tang, and M. J. Brennan, "Design and test of an adjustable quasi-zero stiffness device and its use to suspend masses on a multimodal structure," *Mechanical Systems and Signal Processing*, vol. 152, Article ID 107354, 2021.

[20] G. Gatti, M. J. Brennan, and B. Tang, "Some diverse examples of exploiting the beneficial effects of geometric stiffness nonlinearity," *Mechanical Systems and Signal Processing*, vol. 125, pp. 4–20, 2019.

[21] D. Anastasio and S. Marchesiello, "Experimental characterization of friction in a negative stiffness nonlinear oscillator," *Vibrations*, vol. 3, no. 2, pp. 132–148, 2020.

[22] X. J. Tan, B. Wang, S. W. Zhu et al., "Novel multidirectional negative stiffness mechanical metamaterials," *Smart Materials and Structures*, vol. 29, no. 1, Article ID 015037, 2019.

[23] X. J. Tan, S. Chen, B. Wang, S. W. Zhu, L. Z. Wu, and Y. G. Sun, "Design, fabrication, and characterization of multistable mechanical metamaterials for trapping energy," *Extreme Mechanics Letters*, vol. 28, pp. 8–21, 2019.

[24] S. W. Zhu, B. Wang, L. M. Chen, X. J. Tan, and L. Ma, "Enhance the energy dissipation ability of sleeve-type negative stiffness structures via a phase-difference mechanism," *International Journal of Mechanical Sciences*, vol. 213, Article ID 106803, 2022.

[25] W. S. Robertson, M. R. F. Kidner, B. S. Cazzolato, and A. C. Zander, "Theoretical design parameters for a quasi-zero stiffness magnetic spring for vibration isolation," *Journal of Sound and Vibration*, vol. 326, no. 1-2, pp. 88–103, 2009.

[26] N. Mehreganian, A. S. Fallah, and P. Sareh, "Structural mechanics of negative stiffness honeycomb metamaterials," *Journal of Applied Mechanics*, vol. 88, no. 5, Article ID 051006, 2021.

[27] D. Anastasio, A. Fasana, L. Garibaldi, and S. Marchesiello, "Nonlinear dynamics of a duffing-like negative stiffness oscillator: modeling and experimental characterization," *Shock and Vibration*, vol. 2020, Article ID 3593018, 18 pages, 2020.

[28] P. Balasubramanian, G. Ferrari, and M. Amabili, "Identification of the viscoelastic response and nonlinear damping of a rubber plate in nonlinear vibration regime," *Mechanical Systems and Signal Processing*, vol. 111, pp. 376–398, 2018.

[29] M. Amabili, "Nonlinear damping in large-amplitude vibrations: modelling and experiments," *Nonlinear Dynamics*, vol. 93, no. 1, pp. 5–18, 2018.

[30] F. Alijani, M. Amabili, P. Balasubramanian, S. Carra, G. Ferrari, and R. Garziera, "Damping for large-amplitude vibrations of plates and curved panels, part 1: modeling and experiments," *International Journal of Non-linear Mechanics*, vol. 85, pp. 23–40, 2016.

[31] M. Amabili, F. Alijani, and J. Delannoy, "Damping for large-amplitude vibrations of plates and curved panels, part 2: identification and comparisons," *International Journal of Non-linear Mechanics*, vol. 85, pp. 226–240, 2016.

[32] M. Amabili, "Nonlinear damping in nonlinear vibrations of rectangular plates: derivation from viscoelasticity and experimental validation," *Journal of the Mechanics and Physics of Solids*, vol. 118, pp. 275–292, 2018.

[33] S. Le Guisquet and M. Amabili, "Identification by means of a genetic algorithm of nonlinear damping and stiffness of continuous structures subjected to large-amplitude vibrations. Part I: single-degree-of-freedom responses," *Mechanical Systems and Signal Processing*, vol. 153, Article ID 107470, 2021.

[34] M. Amabili, "Derivation of nonlinear damping from viscoelasticity in case of nonlinear vibrations," *Nonlinear Dynamics*, vol. 97, no. 3, pp. 1785–1797, 2019.

[35] L. Chen, S. Nagarajaiah, and L. Sun, "A unified analysis of negative stiffness dampers and inerter-based absorbers for multimode cable vibration control," *Journal of Sound and Vibration*, vol. 494, Article ID 115814, 2021.

[36] P. Zhou and H. Li, "Modeling and control performance of a negative stiffness damper for suppressing stay cable vibrations," *Structural Control and Health Monitoring*, vol. 23, no. 4, pp. 764–782, 2016.

[37] J. Ahmad, "Influence of negative stiffness damper on stay cable with neoprene rubber bushings," *Journal of Engineering Mechanics*, vol. 147, no. 7, Article ID 04021039, 2021.

[38] I. F. Lazar, S. A. Neild, and D. J. Wagg, "Vibration suppression of cables using tuned inerter dampers," *Engineering Structures*, vol. 122, pp. 62–71, 2016.

[39] H. N. Li, T. Sun, Z. Lai, and S. Nagarajaiah, "Effectiveness of negative stiffness system in the benchmark structural-control problem for seismically excited highway bridges," *Journal of Bridge Engineering*, vol. 23, no. 3, Article ID 04018001, 2018.

[40] S. N. Madhekar and R. S. Jangid, "Use of pseudo-negative stiffness dampers for reducing the seismic response of bridges: a benchmark study," *Bulletin of Earthquake Engineering*, vol. 10, no. 5, pp. 1561–1583, 2012.

[41] M. De Angelis, F. Petrini, and D. Pietrosanti, "Optimal design of the ideal grounded tuned mass damper inerter for comfort performances improvement in footbridges with practical implementation considerations," *Structural Control and Health Monitoring*, vol. 28, no. 9, Article ID e2800, 2021.

[42] A. Salvatore, B. Carboni, and W. Lacarbonara, "Nonlinear dynamic response of an isolation system with superelastic hysteresis and negative stiffness," *Nonlinear Dynamics*, vol. 107, no. 2, pp. 1765–1790, 2022.

[43] M. Wang, S. Nagarajaiah, and F. F. Sun, "Dynamic characteristics and responses of damped outrigger tall buildings using negative stiffness," *Journal of Structural Engineering*, vol. 146, no. 12, Article ID 04020273, 2020.

[44] F. F. Sun, M. Wang, and S. Nagarajaiah, "Multi-objective optimal design and seismic performance of negative stiffness damped outrigger structures considering damping cost," *Engineering Structures*, vol. 229, Article ID 111615, 2021.

[45] F. Petrini, A. Giaralis, and Z. Wang, "Optimal tuned mass-damper-inerter (TMDI) design in wind-excited tall buildings for occupants' comfort serviceability performance and energy harvesting," *Engineering Structures*, vol. 204, Article ID 109904, 2020.

[46] S. Elias and V. Matsagar, "Wind response control of tall buildings with a tuned mass damper," *Journal of Building Engineering*, vol. 15, pp. 51–60, 2018.

[47] J.-Y. Li and S. Zhu, "Versatile behaviors of electromagnetic shunt damper with a negative impedance converter," *IEEE/ASME transactions on Mechatronics*, vol. 23, no. 3, pp. 1415–1424, 2018.

[48] A. A. Taflanidis, A. Giaralis, and D. Patsialis, "Multi-objective optimal design of inerter-based vibration absorbers for earthquake protection of multi-storey building structures," *Journal of the Franklin Institute*, vol. 356, no. 14, pp. 7754–7784, 2019.

[49] H. Li, M. Askari, J. Li, Y. Li, and Y. Yu, "A novel structural seismic protection system with negative stiffness and

controllable damping," *Structural Control and Health Monitoring*, vol. 28, no. 10, Article ID e2810, 2021.

[50] H. Li, Y. Li, and J. Li, "Negative stiffness devices for vibration isolation applications: a review," *Advances in Structural Engineering*, vol. 23, no. 8, pp. 1739–1755, 2020.

[51] H. Li, J. Li, Y. Yu, and Y. Li, "Modified adaptive negative stiffness device with variable negative stiffness and geometrically nonlinear damping for seismic protection of structures," *International Journal of Structural Stability and Dynamics*, vol. 21, no. 08, Article ID 2150107, 2021.

[52] H. Li, Y. Yu, J. Li, and Y. Li, "Analysis and optimization of a typical quasi-zero stiffness vibration isolator," *Smart Structures and Systems*, vol. 27, no. 3, pp. 525–536, 2021.

[53] K. K. Walsh, G. Sallar, J. T. Haftman, and E. P. Steinberg, "Resetting passive stiffness damper with passive negative stiffness device for seismic protection of structures," *Structural Control and Health Monitoring*, vol. 28, no. 8, Article ID e2774, 2021.

[54] K. K. Walsh, "Passive displacement-dependent damper with adjustable stiffness for seismic protection of civil infrastructure," in *Proceedings of the 11th National Conference in Earthquake Engineering*, Los Angeles, CA, USA, June 2018.

[55] J. Wang, C. Zhang, H. Li, and Z. Liu, "Experimental and numerical studies of a novel track bistable nonlinear energy sink with improved energy robustness for structural response mitigation," *Engineering Structures*, vol. 237, Article ID 112184, 2021.

[56] J. Wang, B. Wang, N. E. Wierschem, and B. F. Spencer Jr, "Dynamic analysis of track nonlinear energy sinks subjected to simple and stochastice excitations," *Earthquake Engineering and Structural Dynamics*, vol. 49, no. 9, pp. 863–883, 2020.

[57] H. Iemura and M. H. Pradono, "Application of pseudo-negative stiffness control to the benchmark cable-stayed bridge," *Journal of Structural Control*, vol. 10, no. 3-4, pp. 187–203, 2003.

[58] H. Iemura and M. H. Pradono, "Advances in the development of pseudo-negative-stiffness dampers for seismic response control," *Structural Control and Health Monitoring*, vol. 16, no. 7-8, pp. 784–799, 2009.

[59] H. Iemura, A. Igarashi, M. H. Pradono, and A. Kalantari, "Negative stiffness friction damping for seismically isolated structures," *Structural Control and Health Monitoring*, vol. 13, no. 2-3, pp. 775–791, 2006.

[60] T. Asai, B. F. Spencer Jr, H. Iemura, and C. M. Chang, "Nature of seismic control force in acceleration feedback," *Structural Control and Health Monitoring*, vol. 20, no. 5, pp. 789–803, 2012.

[61] T. W. Sun, L. Y. Peng, X. J. Li, Y. J. Kang, and Y. K. Deng, "Development and analysis of negative stiffness friction damping device," *KSCE Journal of Civil Engineering*, vol. 25, no. 7, pp. 2587–2602, 2021.

[62] T. W. Sun, L. Y. Peng, X. D. Ji, and X. J. Li, "Development of a negative stiffness friction damping device with an amplification mechanism," *Engineering Structures*, vol. 275, Article ID 115286, 2023.

[63] G. P. Cimellaro, M. Domaneschi, and G. Warn, "Three-dimensional base isolation using vertical negative stiffness devices," *Journal of Earthquake Engineering*, vol. 24, no. 12, pp. 2004–2032, 2020.

[64] A. A. Sarlis, D. T. R. Pasala, M. C. Constantinou, A. M. Reinhorn, S. Nagarajaiah, and D. P. Taylor, "Negative stiffness device for seismic protection of structures: shake table testing of a seismically isolated structure," *Journal of Structural Engineering*, vol. 142, no. 5, Article ID 04016005, 2016.

[65] D. T. R. Pasala, A. A. Sarlis, S. Nagarajaiah, A. M. Reinhorn, M. C. Constantinou, and D. Taylor, "Adaptive negative stiffness: new structural modification approach for seismic protection," *Journal of Structural Engineering*, vol. 139, no. 7, pp. 1112–1123, 2013.

[66] S. Nagarajaiah and D. Sen, "Apparent-weakening by adaptive passive stiffness shaping along the height of multistory building using negative stiffness devices and dampers for seismic protection," *Engineering Structures*, vol. 220, Article ID 110754, 2020.

[67] P. Balasubramanian, G. Franchini, G. Ferrari, B. Painter, K. Karazis, and M. Amabili, "Nonlinear vibrations of beams with bilinear hysteresis at supports: interpretation of experimental results," *Journal of Sound and Vibration*, vol. 499, Article ID 115998, 2021.

[68] M. Amjadian and A. K. Agrawal, "A passive electromagnetic eddy current friction damper (PEMECFD): theoretical and analytical modeling," *Structural Control and Health Monitoring*, vol. 24, no. 10, Article ID e1978, 2017.

[69] A. Pall and R. T. Pall, "Performance-based design using pall friction dampers-an economical design solution," in *Proceedings of the 13th World Conference on Earthquake Engineering*, Colombia, Canada, August 2004.

[70] S. Li, B. Wei, H. Tan, C. Li, and X. Zhao, "Equivalence of friction and viscous damping in a spring-friction system with concave friction distribution," *Journal of Testing and Evaluation*, vol. 49, no. 1, Article ID 20190885, 2021.

[71] D. Pietrosanti, M. De Angelis, and A. Giaralis, "Experimental study and numerical modeling of nonlinear dynamic response of SDOF system equipped with tuned mass damper inerter (TMDI) tested on shaking table under harmonic excitation," *International Journal of Mechanical Sciences*, vol. 184, Article ID 105762, 2020.

[72] P. Brzeski, M. Lazarek, and P. Perlikowski, "Experimental study of the novel tuned mass damper with inerter which enables changes of inertance," *Journal of Sound and Vibration*, vol. 404, pp. 47–57, 2017.

[73] Ministry of Housing and Urban-Rural Development of the People's Republic of China, *Code for Seismic Design of Buildings. GB 50011–2010*China Architecture and Building Press, Beijing, China, 2016.